

Effect of Coriolis force on homoclinic bifurcations in thermal convection

Priyanka Maity and Krishna Kumar

Department of Physics and Meteorology, IIT Kharagpur, Kharagpur- 721302, India

Pinaki Pal

Department of Mathematics, National Institute of Technology, Durgapur-713 209, India

(Dated: June 12, 2021)

We present the effects of small Coriolis force on homoclinic gluing and ungluing bifurcations in low-Prandtl-number ($0.025 \leq Pr$) rotating Rayleigh-Bénard system with *stress-free* top and bottom boundaries. We have performed direct numerical simulations for a wide range of Taylor number ($5 \leq Ta \leq 50$) and reduce Rayleigh number r (≤ 1.25). We observe homoclinic ungluing bifurcation, marked by the spontaneous breaking of a larger limit cycle into two possible set of limit cycles in the phase space, for lower values of Ta . Two unglued limit cycles merge together for higher values of Ta , as Ra is raised sufficiently. The range of Ta for which both gluing and ungluing bifurcation can be seen depends on the Prandtl number Pr . The variation of the bifurcation points with Ta is also investigated. We also present a low-dimensional model which qualitatively captures the dynamics of the system near the homoclinic bifurcation points. The model is used to study the variation of the homoclinic bifurcation points with Prandtl number for different values of Ta .

PACS numbers: 47.20.Ky, 47.27.ek, 47.57.-r

I. INTRODUCTION

Nonlinear extended dissipative systems, driven away from equilibrium, reveal a wide range of bifurcations and pattern dynamics [1]. A homoclinic gluing [2] occurs when two limit cycles simultaneously become homoclinic orbits to a single saddle point. This leads to spontaneous merging of two limit cycles to a single limit cycle in the appropriate phase space, as the bifurcation parameter is raised above a critical value. The gluing bifurcation is observed in liquid crystals [3], in fluids [4, 5], and in electronics circuits [6]. Recently, Pal *et. al* [5] showed the possibility of a homoclinic bifurcation in very low-Prandtl-number thermal convection and investigated the pattern dynamics near the bifurcation point.

Rayleigh-Bénard convection (RBC), where a horizontal layer of a fluid is subjected to an adverse temperature gradient, has been widely studied as a model system to investigate interesting pattern dynamics [7], bifurcations [8], route to chaos [9] and turbulence [10]. Low-Prandtl-number convection [11–13], which is relevant in the geophysical [14] and the astrophysical [15] context, show interesting pattern dynamics [16] and a plethora of bifurcations. A uniform rotation about a vertical axis [17, 18], on the other hand, introduces a Coriolis force in the system that breaks the mirror symmetry of the patterns and show several patterns [19]. However, the effect of Coriolis force on homoclinic bifurcations has not been explored.

We present in this article the effect of slow rotation on homoclinic bifurcations and pattern dynamics in its vicinity in low-Prandtl-number RBC using direct numerical simulations (DNS) and a low dimensional model. We observed spontaneous breaking (ungluing) of a larger limit cycle into two limit cycles near a homoclinic point for lower values of Taylor number Ta and again spon-

aneous merger (gluing) of two limit cycles into one at higher values of Ta . We also present a simple model and use it to investigate the Prandtl number dependence of the homoclinic point.

II. THE HYDRODYNAMIC SYSTEM

We consider a thin horizontal layer of Boussinesq fluid of thickness d , kinematic viscosity ν , thermal expansion coefficient α , thermal diffusivity κ , rotating slowly with a uniform angular velocity Ω about a vertical axis, and subjected to an adverse temperature gradient β in the vertical direction. The hydrodynamics of the rotating Rayleigh-Bénard convection is governed by,

$$\partial_t \mathbf{v} + (\mathbf{v} \cdot \nabla) \mathbf{v} = -\nabla p + Ra\theta \boldsymbol{\lambda} + \nabla^2 \mathbf{v} + \sqrt{Ta}(\mathbf{v} \times \boldsymbol{\lambda}), \quad (1)$$

$$Pr[\partial_t \theta + (\mathbf{v} \cdot \nabla)\theta] = \nabla^2 \theta + v_3, \quad (2)$$

$$\nabla \cdot \mathbf{v} = 0, \quad (3)$$

where $\mathbf{v}(x, y, z, t) \equiv (v_1, v_2, v_3)$, $\theta(x, y, z, t)$ and $p(x, y, z, t)$ are respectively the flow velocity, the convective temperature field and the convective pressure field. The unit vector $\boldsymbol{\lambda}$ is directed opposite to the direction of the gravitational acceleration \mathbf{g} . In the above equations all the length scales are made dimensionless by the fluid thickness d , the time scale by the viscous diffusive time d^2/ν , and the temperature field by $\nu\beta d/\kappa$. The dimensionless parameters are: Rayleigh number $Ra = (g\alpha\beta d^4)/(\nu\kappa)$, Prandtl number $Pr = \nu/\kappa$ and Taylor number $Ta = 4\Omega^2 d^4/\nu^2$. In the limit $Pr \rightarrow 0$, eq. 2 is slaved to the vertical velocity, i.e., $\nabla^2 \theta = -v_3$. We consider thermally conducting and *stress-free* bounding surfaces. This leads to the boundary conditions $\theta = \partial_z v_1$

Convective patterns	$Pr = 0$		$Pr = 0.025$	
	$r(Ta = 10)$	$r(Ta = 40)$	$r(Ta = 10)$	$r(Ta = 25)$
STO	1.001 - 1.018	1.001 - 1.071	1.001 - 1.02	1.001 - 1.021
STC	1.019 - 1.088	1.072 - 1.116	-	1.022 - 1.037
OCR -II'	-	1.117 - 1.127	-	1.038 - 1.139
OCR-I	1.089 - 1.120	1.128 - 1.154	1.051 - 1.148	1.140 - 1.175
OCR-II	1.121 - 1.137	1.155 - 1.163	1.149 - 1.168	1.176 - 1.186
CR	1.138 - 1.187	1.164 - 1.183	1.170 - 1.210	1.187 - 1.209
SQ	≤ 1.189	≤ 1.184	≤ 1.211	≤ 1.210

TABLE I. Flow patterns observed in DNS for different regions of r for two values of Pr . The patterns are: Self-tuned periodic competition of rolls (STO), chaotic competition of self-tuned rolls (STC), oscillating cross-rolls with $|W_{101}| = |W_{011}|$ (OCR-I), oscillating cross-rolls with $|W_{101}|_{max} \neq |W_{011}|_{max}$ (OCR-II and OCR -II'), stationary cross-rolls (CR) ($W_{101} = W_{011}$) and stationary squares (SQ) ($W_{101} \neq W_{011}$).

$= \partial_z v_2 = v_3 = 0$ on the boundaries located at $z = 0$ and 1. All the convective fields are assumed to be periodic in horizontal plane. The direct numerical simulations (DNS) of the hydrodynamic system (eqs. 1-3) with the boundary conditions is carried out using an open-source code TARANG [20] based on pseudo spectral method. All the convective fields are expressed as:

$$\Psi(x, y, z, t) = \sum_{l,m,n} \Psi_{lmn}(t) e^{ik(lx+my)} f_n(z),$$

$$\Phi(x, y, z, t) = \sum_{l,m,n} \Phi_{lmn}(t) e^{ik(lx+my)} g_n(z), \quad (4)$$

where $\Psi(x, y, z, t) \equiv (v_1, v_2, p)^T$, $f(z) = \sin(n\pi z)$ and $\Phi(x, y, z, t) \equiv (v_3, \theta)^T$, $g(z) = \cos(n\pi z)$. We consider a periodic box of size $2\pi/k : 2\pi/k : 1$ with $k = k_c(Ta)$ for our simulations. $k_c(Ta)$ is the critical wave number predicted by linear theory [17]. The spatial grid resolution of $64 \times 64 \times 64$ is used for DNS, which is quite good to resolve the flow structure near onset. The time advancement is done using standard fourth order Runge-Kutta (RK4) integration scheme. The time step used for integration varies in the range $0.0005 \leq dt \leq 0.001$. We started our simulations with random initial conditions by fixing the values of Prandtl number and Taylor number. The reduced Rayleigh number $r = Ra/Ra_c(Ta)$, where Ra_c is the critical Rayleigh number predicted by the linear theory of Chandrasekhar [17], is increased from 1 in small steps of $0.001 \leq \Delta r \leq 0.01$. Reduced Rayleigh number has been varied in the range $1 \leq r \leq 1.25$ for all values of Ta mentioned above. The values at the final time step has also been used as the initial condition for the next run. We have performed our runs for Taylor numbers $2 \leq Ta \leq 50$ for various values of Prandtl numbers. The case of $Pr \rightarrow 0$ and $Pr = 0.025$ have been studied in details. We have also performed runs by starting with a higher value of r and then decreasing the r in small steps. We have not observed any hysteresis in the range of r considered here.

The various flow patterns observed for two different values of Prandtl numbers ($Pr = 0$ and 0.025) for different values of Ta are listed in table I. The onset of convection is always self-tuned oscillations (STO) of two

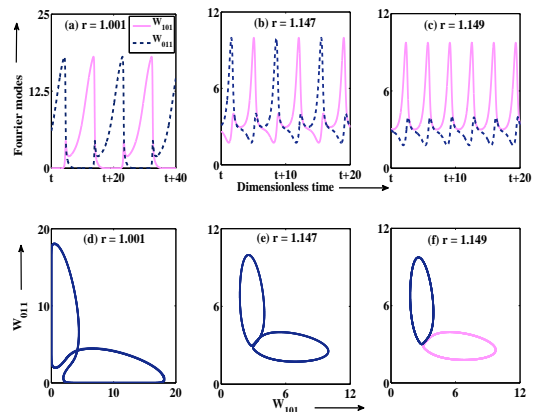


FIG. 1. (Colour online) Behaviour near the homoclinic bifurcation for $Ta = 10$ at $Pr = 0.025$ from DNS: The temporal variation of Fourier modes W_{101} (pink (gray) solid lines) and W_{011} (blue (black) dotted lines) for (a) $r = 1.001$, (b) $r = 1.147$, and (c) $r = 1.149$. The onset is non-local solution with a periodic competition between two mutually perpendicular set of self-tuned rolls(STO). The corresponding phase portraits on $W_{101} - W_{011}$ plane are plotted in (d), (e), and (f) respectively.

mutually perpendicular set of rolls. The temporal variation of the leading Fourier modes (W_{101} and W_{011}) in STO, OCR-I, and OCR-II states at $Ta = 10$ and $Pr = 0.025$ are plotted in first row of fig. 1. In STO state both the modes (W_{101} and W_{011}) oscillate with zero minima and a phase difference (fig. 1 (a)). The mode W_{101} (rolls along y-axis) remains zero as the mode W_{011} (rolls along x-axis) grows from a minimum value. When W_{011} grows to a large value W_{101} starts growing and simultaneously W_{011} drops to a minimum. W_{011} remains zero within a period when W_{101} is growing and again starts growing from the minima in the vicinity of the time when W_{101} attains a maxima. This self tuning repeats periodically and is similar to the self tuning of rolls observed by Kumar, Fauve, and Thual [13]. As r is raised, periodic self tuned oscillations become chaotic (STC) in nature.

With further increase in r we reach the oscillating cross rolls (OCR-I, $|W_{101}| = |W_{011}|$) state where two mutually perpendicular set of cross-rolls start oscillating with non-zero minimum (see fig. [?] (b)). Both the STO and OCR-I states represent nonlocal solutions, with existence of one large limit cycle (as shown in figs. [?] (d) and (e)). When r is increased further beyond a certain critical value r_{ug} we reach OCR-II state. In this state, the mutually perpendicular set of oscillating cross rolls break into two possible set of oscillating cross roll solutions (one with $|W_{101}| > |W_{011}|$ and another with $|W_{101}| < |W_{011}|$). The temporal variation of the Fourier modes in this state is shown in fig. 1 (c) and the corresponding phase portrait is shown in fig. 1 (f). We observe the existence of two limit cycles (represented by the blue (black) and pink (gray) in fig. 1 (f)) in OCR-II state. The transition from a larger limit cycle to either of the two possible smaller limit cycles is via homoclinic ungluing bifurcation with a divergence in time period of oscillation near the bifurcation. The two limit cycle gradually diminishes in size with the increment of r and ultimately reaches the stationary cross roll (CR, $W_{101} \neq W_{011}$) solutions when r is raised above a critical value r_1 . The transition OCR-II \rightarrow CR is via an inverse Hopf bifurcation. The CR state further bifurcates to the stationary square (SQ, $W_{101} = W_{011}$) solution when r exceeds the critical value r_2 via an inverse pitchfork.

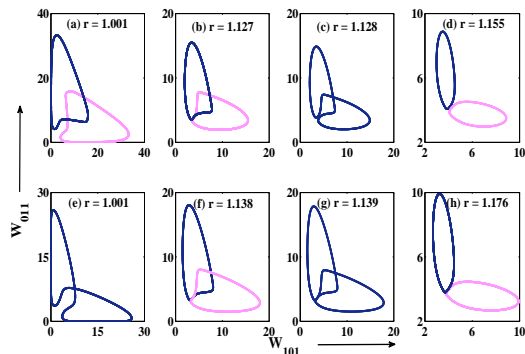


FIG. 2. (Colour online) Phase portraits displaying homoclinic gluing and homoclinic ungluing bifurcations from DNS: The first row shows the phase projections for $Pr = 0$ at $Ta = 40$ for (a) $r = 1.001$, (b) $r = 1.127$, (c) $r = 1.128$ and (d) $r = 1.155$. The second row shows the phase projections for $Pr = 0.025$ and $Ta = 25$ for (e) $r = 1.001$, (f) $r = 1.138$, (g) $r = 1.139$ and (h) $r = 1.176$.

For higher values of Ta , however we observe the presence of both homoclinic ungluing and homoclinic gluing occurring with variation of r . The presence of both gluing and ungluing bifurcation is observed in the range $40 \leq Ta \leq 50$ for $Pr = 0$, and for $25 \leq Ta \leq 35$ for $Pr = 0.025$. Figure 2 describes the phase portraits on $W_{101} - W_{011}$ plane showing the occurrence of successive homoclinic gluing and ungluing bifurcation. The upper row of figure 2 is for $Pr = 0$ at $Ta = 40$ and the lower

row is for $Pr = 0.025$ at $Ta = 25$. The onset is self-tuned (STO) as observed in lower values of Ta . For $Pr = 0$ case the onset is local solution with presence of two limit cycles as shown in fig. 2(a). Whereas for $Pr \neq 0$ the onset is non-local solution with existence of one larger limit cycle (fig. 2(e)) as observed for lower values of Ta previously. The phase projections of STO, OCR-II', OCR-I, and OCR-II states on $W_{101} - W_{011}$ plane are displayed in first, second, third, and fourth column of fig. 2 respectively. With increment of r the system enter into chaotic state and the next ordered state appears in the form of OCR-II' solution with further increase of r . The OCR-II' solution is similar to OCR-II state, with presence of two limit cycles marked by blue (black) and pink (gray) lines, described earlier but is not present for lower values of Taylor numbers. In this state the modes oscillates W_{101} and W_{011} oscillates with a non zero minimum and unequal amplitudes ($|W_{101}| \neq |W_{011}|$) with a constant phase difference. As r is increased above a critical value r_g , the two limit cycles spontaneously merge to form a bigger limit cycle and the system bifurcates to OCR-I state via a homoclinic gluing bifurcation. All the subsequent bifurcations are similar to he sequence observed for lower values of Ta described earlier.

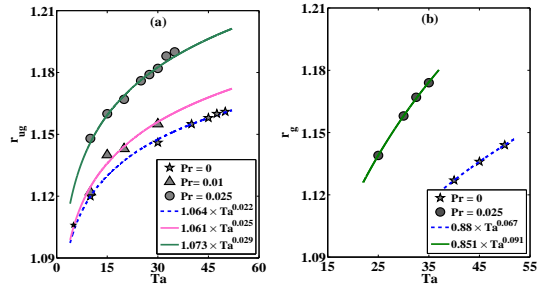


FIG. 3. (Colour online) Variation of homoclinic bifurcation points with Taylor number Ta as obtained from DNS: The variation of r_{ug} with Ta for three values of Prandtl numbers ($Pr = 0$, $Pr = 0.01$, and $Pr = 0.025$) are plotted in (a). The points marked by 'o', ' Δ ' and ' \star ' represent the data for $Pr = 0$, $Pr = 0.01$ and $Pr = 0.025$ respectively. Variation of homoclinic gluing bifurcation point r_g with Ta for $Pr = 0$ and $Pr = 0.025$ is plotted in (b). Both r_{ug} and r_g shows power law dependence on Ta .

The value of r at which homoclinic bifurcations occurs depends on Taylor number for a fixed Prandtl number. The dependence of homoclinic bifurcation points on Ta is plotted in fig. 3. The homoclinic ungluing bifurcation point r_{ug} , where transition from OCR-I \rightarrow OCR-II take place, shows power law dependence on Ta (fig. 3(a)). The point r_{ug} varies as Ta^γ with $\gamma = 0.022$ for $Pr = 0$, $\gamma = 0.025$ for $Pr = 0.01$, and $\gamma = 0.029$ for $Pr = 0.025$. The transition from OCR-II' \rightarrow OCR-I occurs at $r = r_g$ only for higher values of Ta . Figure 3(b) shows the variation in r_g as Taylor number is varied gradually. The bifurcation point r_g also shows power law dependence on Ta with $r_g \propto Ta^\beta$. The values of β for $Pr = 0$ and $Pr = 0.025$

are 0.067 and 0.091 respectively. The value of Taylor number upto which gluing or ungluing can be observed also depend on the value of Pr. Presence of gluing or ungluing bifurcation is observed only for $Ta \leq 50$ at Pr = 0 and for $Ta \leq 35$ at Pr = 0.025.

III. THE MODEL

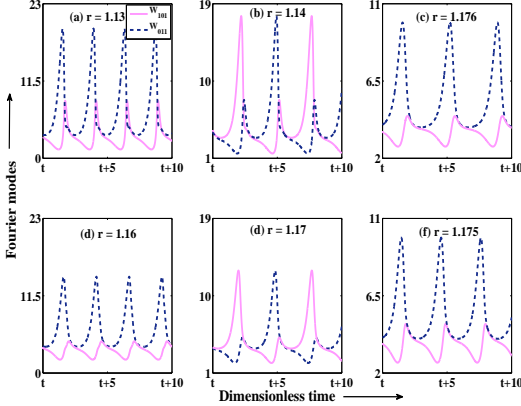


FIG. 4. (Colour online) Comparison of DNS and model for Pr = 0.025 and Ta = 25: The temporal behaviour of leading Fourier modes W_{101} (pink (gray) solid lines) and W_{011} (blue (black) dotted lines) for (a) $r = 1.13$, (b) $r = 1.14$ and (c) $r = 1.176$ as obtained from DNS are plotted in upper row of the figure. The lower row displays the time signal as obtained from model for (d) $r = 1.16$, (e) $r = 1.17$, and (f) $r = 1.175$. The model can qualitatively captures the temporal variation of the modes in OCR-II', OCR-I, and OCR-II state (represented in first, second, and third column respectively).

Direct numerical simulations are enormously time consuming and requires huge computation facilities. Hence we try to capture the system using a few mode model, derived using Galerkin method [13]. For this purpose we expand the convective fields as sine and cosine functions in compatible with the boundary conditions as follows:

$$\Phi = \sum_{l,m,n} [\Phi_{lmn}(t) \cos lk_c x \cos mk_c y + \Phi_{\bar{l}\bar{m}\bar{n}}(t) \sin lk_c x \sin mk_c y] g(z), \quad (5)$$

where, $g(z) = \sin(n\pi z)$ for vertical velocity v_3 and convective temperature field θ expansion and $g(z) = \cos(n\pi z)$ for vertical vorticity ($\omega_3 = (\nabla \times \mathbf{v}) \cdot \boldsymbol{\lambda}$) expansion. We choose the following eight real vertical velocity (v_3) modes: $\bar{W}_{101}, \bar{W}_{011}, \bar{W}_{112}, \bar{W}_{\bar{1}\bar{1}\bar{2}}, \bar{W}_{211}, \bar{W}_{2\bar{1}\bar{1}}, \bar{W}_{121}, \bar{W}_{\bar{1}\bar{2}\bar{1}}$, twelve real vertical vorticity (ω_3) modes: $\bar{Z}_{101}, \bar{Z}_{011}, \bar{Z}_{112}, \bar{Z}_{\bar{1}\bar{1}\bar{2}}, \bar{Z}_{211}, \bar{Z}_{2\bar{1}\bar{1}}, \bar{Z}_{121}, \bar{Z}_{\bar{1}\bar{2}\bar{1}}, \bar{Z}_{\bar{1}\bar{1}\bar{0}}, \bar{Z}_{200}, \bar{Z}_{020},$ and \bar{Z}_{220} , and nine real modes for temperature field θ : $\bar{\theta}_{101}, \bar{\theta}_{011}, \bar{\theta}_{112}, \bar{\theta}_{\bar{1}\bar{1}\bar{2}}, \bar{\theta}_{211}, \bar{\theta}_{2\bar{1}\bar{1}}, \bar{\theta}_{121}, \bar{\theta}_{\bar{1}\bar{2}\bar{1}},$ and $\bar{\theta}_{002}$. We then project the expansion on eqs. 1 and 2 to obtain a twenty nine mode model consisting of twenty-nine coupled first ordered non-linear differential equations. In the

limit Pr $\rightarrow 0$, the temperature modes θ becomes slaved to v_3 via $\nabla^2 \theta = -v_3$ and the model reduces to a twenty mode model except the θ modes.

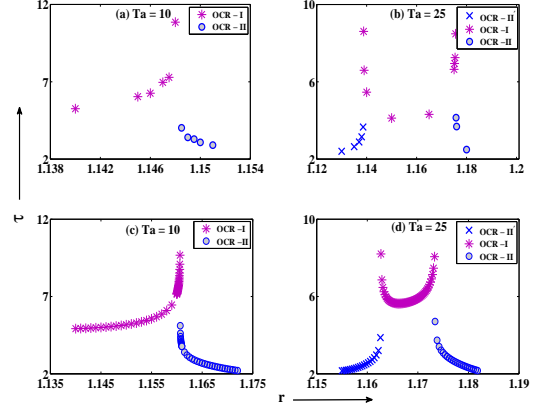


FIG. 5. (Colour online) Variation of dimensionless time period (τ) with r near the homoclinic bifurcation points:(a) $Ta = 10$ and (b) $Ta = 25$ shows the divergence of time period of oscillations near the homoclinic bifurcation points as obtained from DNS for . The lower row of the figure shows similar behaviour for (c) $Ta = 10$ and (d) $Ta = 25$ as obtained from model. The data for OCR-II', OCR-I, and OCR-II are denoted by points marked as 'x', '*', and 'o' respectively. The data from DNS and model are in good agreement with each other.

The model can capture all the bifurcations observed in DNS qualitatively well. The model is quite good for lower values of Taylor number and shows deviation from DNS for higher values. We observe presence ungluing bifurcation in the model for $2 \leq Ta \leq 50$ at Pr = 0 and for $2 \leq Ta \leq 25$ for Pr = 0.025. But homoclinic gluing bifurcation is observed only for higher values of Ta which is consistent with DNS. The model shows gluing bifurcation for $35 \leq Ta \leq 50$ at Pr = 0 and for $15 \leq Ta \leq 25$ for Pr = 0.025. Figure 4 compares the time series obtained from DNS and the model for Ta = 25 at Pr = 0.025. The upper row of fig 4 shows the temporal behaviour of the modes W_{101} and W_{011} in OCR-II' (fig. 4(a)), OCR-I (fig. 4(b)), and OCR-II (fig. 4(c)) as obtained from DNS. The corresponding time series from model is plotted in the lower row of the figure. The model can qualitatively capture the temporal behaviour as obtained from DNS. Figure 5 displays the variation in time period of oscillations (τ) with r as observed from DNS (upper row) and model (lower row) at Pr = 0.025 for Ta = 10 and Ta = 25. The time period diverges near the homoclinic bifurcation points.

Now we use the model to capture the sequence of bifurcations observed in DNS. The bifurcation diagram for Ta = 10 at Pr = 0.025 is plotted in fig. 6(a). The model shows existence of all the flow patterns observed in DNS except the self-tuned chaotic region (STC). We observe two types of fixed point solutions, SQ ($|W_{101}| = |W_{011}|$)

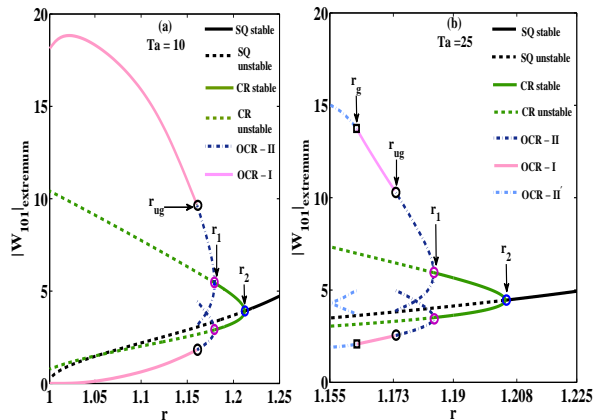


FIG. 6. (Colour online) Linear stability analysis for $Pr = 0.025$ at $Ta = 10$ and $Ta = 25$: (a) displays the bifurcation diagram with variation of r as the parameter for $Ta = 10$. It captures STO, OCR-I, OCR-II, CR, and SQ states as r is varied in small steps. The bifurcation diagram obtained for $Ta = 25$ is plotted in (b). The bifurcation diagram captures OCR-II' solution in addition to all the other state mentioned in (a). The transition from OCR-II' \rightarrow OCR-I takes place at $r = r_g$ (represented by black square in the figure)

and CR ($|W_{101}| \neq |W_{011}|$) in the bifurcation diagram. The SQ solutions are displayed by green (dark gray) lines, while CR solution are marked by the black lines. The stable and unstable fixed point solutions are represented by the solid and dashed lines respectively. Square fixed point are observed in the range $1.212 \leq r \leq 1.25$ and they becomes unstable for $1.212 < r$, but continues to exist as saddle point till $r = 1$. Stationary cross rolls solutions are stable for $1.179 \leq r \leq 1.211$ and becomes unstable for $r < 1.179$. Thus, we do not observe any fixed point solution at the onset.

The onset of convection is self tuned oscillations with $|W_{101}| = |W_{011}|$. The STO solutions converts to OCR-I solutions as r is increased and the minimum of oscillation becomes non-zero. The global extrema of STO and OCR-I solutions are represented by the pink (light gray) solid lines. This transition takes place approximately for $1.05 \leq r$. As r is increased gradually the single limit cycle in OCR-I state comes closer and closer to the saddle fixed point. When r is raised above the critical value $r_{ug} = 1.161$ (marked by the blue (black) circle in fig 6(a)) the system bifurcates to OCR-II state. The two branches of OCR-II solutions are represented as blue (black) dashed-dotted lines. At the bifurcation point the limit cycle becomes homoclinic orbit to the saddle fixed point and the time period diverges. The bigger limit cycle spontaneously breaks into two smaller limit cycle and the system evolves to OCR-II state. The bifurcation from OCR-I to OCR-II takes via homoclinic ungluing bifurcation. Both the existing limit cycles shrink in size as r is raised higher and the system bifurcates to CR takes place at $r = r_1$ via inverse Hopf bifurcation. The CR state fur-

ther bifurcates to SQ solutions at $r = r_2$ via an inverse pitchfork.

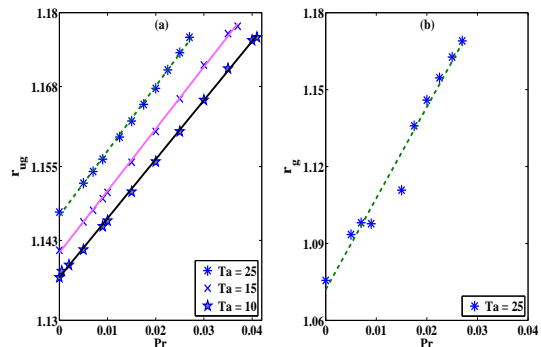


FIG. 7. Variation of homoclinic bifurcation points with Pr for a fixed value of Taylor number as obtained from model: The variation of homoclinic ungluing point r_{ug} with Prandtl number for three different values of Taylor number ($Ta = 10, 15$, and 25) are plotted in (a). The points marked by ‘ \star ’, ‘ \times ’, and ‘ $*$ ’ denotes the data for $Ta = 10, Ta = 15$, and $Ta = 25$ respectively. The variation of homoclinic gluing bifurcation point r_g with Pr for $Ta = 25$ is plotted in (b).

At higher value of Ta , we observe presence of both gluing and ungluing bifurcation as seen in DNS. The bifurcation diagram for $Pr = 0.025$ at $Ta = 25$ is plotted in fig. 6(b). We presence of OCR-II' state in addition to all the other states observed for $Ta = 10$ case. The model shows chaos at the onset while STO solutions were observed in DNS. The first ordered state in the model appears as the OCR-II' ($|W_{101}| = |W_{011}|$) solutions. The two branches of OCR-II' state are marked by the light blue (light gray) dashed-dotted lines. The SQ fixed point solution to be stable for $1.205 \leq r \leq 1.25$ and becomes saddle fixed points $1.205 < r$. Whereas the CR solutions are stable for $1.184 \leq r \leq 1.204$ and becomes unstable for $1.184 < r$. The two branches of OCR-II' comes nearer to the saddle fixed point as r is increases in small steps. The one of the branches touch the saddle point the two limit cycle of OCR-II' state simultaneously becomes homoclinic orbit to the saddle point. The two limit cycle then spontaneously merge to form a bigger limit cycle which now avoids the saddle point and the system reaches OCR-I state. The transition from OCR-II' \rightarrow OCR-I state occurs via homoclinic gluing bifurcation when r is raised above the critical value r_g (represented as the blue (black) square in fig. 6). All the other bifurcations are similar as in case of $Ta = 10$. Variation of homoclinic bifurcation points r_g and r_{ug} with Prandtl number is plotted in fig. 7. Both the homoclinic bifurcation points (r_{ug} and r_g) show linear dependence on Pr . The point r_{ug} increases linearly with Pr with a slope close to 1 (fig. 7 (a)), while r_g varies with a slope equal to 3.65 (fig. 7 (b)).

IV. CONCLUSIONS

We have investigated the effect of Coriolis force on homoclinic bifurcation in RBC. We have found existence of ungluing bifurcation for all values of Taylor numbers, while gluing bifurcation exists on for higher valued of Ta. The values of homoclinic bifurcations points increases as Taylor number is increased at a fixed value of Prandtl number. No gluing or ungluing bifurcation is observe in DNS for Prandtl number greater than 0.04. We have also derived a low dimensional model which can capture the homoclinic bifurcations quite well and n addition can

also explain the bifurcations occurring in DNS for higher values of r. The model shows that the homoclinic bifurcations points have linear dependence on the Prandtl number for a fixed values of Ta. We do not observe any homoclinic bifurcations in the model for $0.041 \leq Pr$.

ACKNOWLEDGMENTS

We benefited from fruitful discussions with Pinaki Pal, H. Pharasi and A. Basak.

-
- [1] Petrossian A., Pinard M., Maître A., Courtois J.-Y., and Grynberg G., *Europhys. Lett.*, **18** 689 (1992); Luding S., Clément E., Rajchenbach J., and Duran J., *Europhys. Lett.*, **036247** (1996); Cross M. C. and Hohenberg P. C., *Rev. Mod. Phys.*, **65** 851 (1993).
- [2] Coste J. and Peyraud N., *Phys. Lett.*, **84A** 17 (1981); Coste J. and Peyraud N., *Physica D*, **11** 25 (1984); Gambaudo J. M., Glendinning P. A., and Tresser C., *J. Phys. Lett. (France)*, **46** L653 (1985); Gambaudo J. M., Procaccia I., Thomae S., and Tresser C., *Phys. Rev. Lett.*, **57** 925 (1986).
- [3] Demeter G. and Kramer L., *Phys. Rev. Lett.*, **83** 4744 (1999); Peacock T. and Mullin T., *J. Fluid Mech.*, **432** 369 (2001).
- [4] Meron E. and Procaccia I., *Phys. Rev. A*, **35** 4008 (1987); Lopez J. M. and Marques F., *Phys. Rev. Lett.*, **85** 972 (2000); Abshagen J., Pfister G., and Mullin T., *Phys. Rev. Lett.*, **87** 224501 (2001).
- [5] Pal P., Kumar K., Maity P., and Dana S. K., *Phys. Rev. E.*, **87** 023001 (2013).
- [6] Glendinning P., Abshagen J., and Mullin T., *Phys. Rev. E*, **64** 036208 (2001); Roy P.K. and Dana S.K., *Int. J. Bifurcation Chaos*, **16** 3497 (2006).
- [7] Daviaud F., Dubois M., and Bergé P., *Europhys. Lett.*, **9** 441 (1989); Assenheimer M. and Steinberg V., *Nature*, **367** 345 (1994); Silber M. and Proctor M.R.E., *Phys. Rev. Lett.*, **81** 2450 (1998); Demircan A. and Seehafer N., *Europhys. Lett.*, **53** 202 (2001).
- [8] Gauthier S., Gamess A., and Iooss G., *Europhys. Lett.*, **13** 117 (1990); Ecke R. E., Zhong F., and Knobloch E., *Europhys. Lett.*, **19** 177 (1992);
- [9] Giglio M., Musazzi S., and Perini, U., *Phys. Rev. Lett.*, **47** 243 (1981); Maganza C. and Caussé R., *Europhys. Lett.*, **1** 295 (1986); Bauer M. and Martienssen W., *Europhys. Lett.*, **10** 427 (1989); Xi H.-W., Li X.-J., and Gunton J. D., *Phys. Rev. Lett.*, **78** 1046 (1997).
- [10] King E. M., Stellmach S., Noir J., Hansen U., and Aurnou J. M., *Nature*, **457** 07647 (2009); Pharasi H. K., Kannan R., Kumar K. and Bhattacharjee J. K., *Phys. Rev. E.*, **84** 047301 (2011).
- [11] Busse F. H., *J. Fluid Mech.*, **52** 97 (1972); Roche P.-E., Castaing B., Chabaud B., and Hébral B., *Europhys. Lett.*, **58** 693 (2002); Chiffaudel A., Fauve S., and Perrin B., *Europhys. Lett.*, **4** 555 (1987).
- [12] Thual O., *J. Fluid Mech.*, **240** 229 (1992); Kumar K., Pal P., and Fauve S., *Europhys. Lett.*, **74** 1020 (2006); Pal P., Wahi P., Paul S., Verma M. K., Kumar K., and Mishra P. K., *Europhys. Lett.*, **87** 54003 (2009); Mishra P. K., Wahi P., and Verma, M. K., *Europhys. Lett.*, **89** 44003 (2010).
- [13] Kumar K., Fauve S., and Thual O., *J. Phys. II*, **6** 945 (1996).
- [14] Glatzmaier G. A., Coe R. S., Hongre L., and Roberts P. H., *Nature*, **401** 885-890 (1999).
- [15] Cattaneo F., Emonet T., and Weiss N., *Astrophys. J.*, **588** 1183 (2003); Miesch M. S., *Sol. Physics*, **192** 59 (2000).
- [16] Clever R. M. and Busse F. H., *J. Fluid. Mech.*, **176** 403 (1987); Hu Y., Ecke R. E., and Ahlers G., *Phys. Rev. Lett.*, **72** 2191 (1994); Hu Y., Pesch W., Ahlers G., and Ecke R. E., *Phys. Rev. E*, **58** 5821 (1998); Pal P. and Kumar K., *Phys. Rev. E*, **65** 047302 (2002).
- [17] Chandrasekhar S., *Hydrodynamic and Hydromagnetic stability.*, Dover publications, New York, 1961 1-143.
- [18] Rossby H. T., *J. Fluid. Mech.*, **36** 309 (1969).
- [19] Küppers G. and Lortz D., *J. Fluid Mech.*, **35** 609 (1969); Bajaj K. M. S., Liu J., Naberhuis B., and Ahlers G., *Phys. Rev. Lett.*, **81** 806-809 (1998); Guarino A. and Vidal V., *Phys. Rev. E*, **69** 066311 (2004).
- [20] Verma, M.K., Object-oriented Pseudo-spectral code TARANG for turbulence simulation arXiv:1103.2517 [pdf, other]2011